Geophysical Journal International

Geophys. J. Int. (2012) **188,** 583–599 doi: 10.1111/j.1365-246X.2011.05276.x

New insights into the application of the Coulomb model in real-time

Flaminia Catalli[1,2] and Chung-Han Chan[1,3]

[1] *GFZ German Research Centre for Geosciences, Section 2.6 Seismic Hazard and Stress Field, Potsdam, Germany. E-mail: flaminia.catalli@sed.ethz.ch*
[2] *Swiss Seismological Service, Institute of Geophysics, ETH, Zürich, Zürich, Switzerland*
[3] *Department of Geosciences, National Taiwan University, Taipei, Taiwan*

Accepted 2011 October 18. Received 2011 September 30; in original form 2010 June 14

SUMMARY

The Coulomb model for stress change estimation is considered one of the most powerful physics-based forecasting tools, even though its calculations are affected by uncertainties due to the large number of *a priori* assumptions needed. The aim of this paper is to suggest a straightforward and reliable strategy to apply the Coulomb model for real-time forecasting. This is done by avoiding all dispensable assumptions, thus reducing the corresponding uncertainties. We demonstrate that the depth at which calculations are made is a parameter of utmost importance and apply the Coulomb model to three sequences in different tectonic regimes: Umbria-Marche (normal), Landers (strike-slip), and Chi–Chi (thrust). In each case the results confirm that when applying the Coulomb model: (i) the depth of calculation plays a fundamental role; (ii) depth uncertainties are not negligible; (iii) the best forecast at a given location is obtained by selecting the maximum stress change over the whole seismogenic depth range.

Key words: Earthquake interaction, forecasting, and prediction.

1 INTRODUCTION

Improving earthquake forecasting is important to meet the need to give society reliable measures for disaster prevention and mitigation. In the last decade, several international projects were launched to initiate scientific prediction experiments, for example, CSEP—Collaboratory for the Study of Earthquake Predictability—(Jordan 2006); RELM—Regional Earthquake Likelihood Models—(Field 2007); SAFER—Seismic early warning For EuRope—(www.saferproject.net); NERIES—Network of Research Infrastructures for European Seismology—(www.neries-eu.org). These experiments have sought to test and compare the forecasting ability of a range of purely statistical and physical prediction models. The optimistic final goal is to create a worldwide reliable warning system based on effective and robust models.

The number of uncertainties associated with free parameters and model assumptions is generally larger for physics-based than for empirical statistical models. This has lead to the conclusion that statistical models perform better than physics-based ones (Wössner *et al.* 2011). However, the Coulomb Failure Function (CFF) model for stress transfer and triggering is one physical model that has been applied in practice, even to the point of guiding public alerts (Steacy *et al.* 2005a). Earthquake interaction and aftershock occurrence are commonly well modeled as the response to Coulomb stress change induced by previous events (King *et al.* 1994; Harris 1998; Stein 1999; King & Cocco 2001; Steacy *et al.* 2005a among many others). In spite of these successful applications, there are several uncertainties in the CFF model that require further study of the robustness of the model itself. Many recent papers are devoted to sensitivity studies of CFF-based physical models with the aim to develop more reliable and practical model settings (Catalli *et al.* 2008; Hainzl *et al.* 2009; Cocco *et al.* 2010; Hainzl *et al.* 2010a,b; Chan *et al.* 2010). The common concern of such studies is the need to make models more competitive in terms of dependability and pragmatism, so that they may be applied in real time.

The main elements that enter into the calculation of Coulomb stress changes (ΔCFF) are location and geometry of both source and receiver faults as well as the slip distribution on the source plane. The fault geometries are described by strike, dip and rake of the respective focal mechanisms. Concerning slip distribution, Steacy *et al.* (2004) show that stress and slip heterogeneities, which are difficult to estimate, as well as heterogeneity of the rock precondition, can significantly influence stress calculations (Marsan 2006; Hainzl & Marsan 2008). It has been shown that accounting for small-scale variability can explain the absence of regions of quiescence in the first part of the aftershock activity (Helmstetter & Shaw 2006; Marsan 2006). This small-scale variability can be related to fractal slip on the mainshock rupture plane, heterogeneous pre-stress, or material conditions. In a rigorous retrospective forecast experiment conducted on the 1992 Landers sequence, Wössner *et al.* (2011) have clearly shown that those CFF-based models that do not predict any stress shadow perform better than the others. This result suggests that elements of stochasticity need to be included in the physics-based models in order to reflect the large uncertainties in stress calculations. However, the focus of this paper is the influence of locations and fault geometries on ΔCFF. Chan & Ma (2004) and

Steacy *et al.* (2004) show the importance of well-constrained fault geometries, independently of the details of slip on the rupture plane, in order to estimate mainshock-aftershock stress triggering. Generally, strike, dip and rake of the source fault are known. On the other hand, the degree to which these parameters can be estimated for the receiver faults has a profound influence on the uncertainties of the resulting stress change distribution, and various strategies have been proposed to address this problem. McCloskey *et al.* (2003), and then Steacy *et al.* (2005b), suggested that meaningful calculations of Coulomb stress could be made, provided that the planes onto which stresses are to be resolved are well constrained. Stress is typically calculated for two idealized cases: (i) fixed receiver fault mechanism, that is fixed strike, dip, and rake angles, or (ii) optimally oriented planes (OOPs, as usually referred to in the literature), assuming that earthquakes will be triggered only on those planes with maximum total Coulomb stress. In both cases, earthquake nucleation is considered only to occur on a fault with one particular orientation and this assumption is rather unrealistic. The seismogenic crust is typically fractured in a complex way, and thus potential receiver faults, on which earthquakes can nucleate, have a distribution of orientations (McCloskey *et al.* 2003). Moreover, Coulomb stress changes computed for OOPs are associated with theoretical focal mechanisms, which might not exist in reality, in particular in the near field where the stress field is strongly influenced by the unresolved mainshock slip (Nostro *et al.* 2005; Hainzl *et al.* 2010b). Recently, Hainzl *et al.* (2010a) suggested that more realistically earthquakes can nucleate with some probability on all faults existing in the rock volume, depending only on the specific stressing rate. Thus, for Coulomb stress calculation they suggested considering a random orientation of receiver faults using a distribution function. In accordance with the findings of McCloskey *et al.* (2003) and of Hainzl *et al.* (2010a), we follow the approach of Toda *et al.* (2008) and Chan *et al.* (2010) by considering spatially variable receiver faults that match the nearest available reference focal mechanism.

In this paper, we are particularly interested in studying the influence due to calculation depth for Coulomb stress estimations. The relative locations of source and receiver faults are important in two ways: first, in order to compare calculated stress changes with observed aftershocks, and secondly because the distribution of induced stress changes depends strongly on the depth for which these stress changes are calculated. In the literature stress calculations are generally estimated at a fixed depth (i.e. the representative depth for the studied seismogenic volume) or, in more recent works (Hainzl *et al.* 2009 and 2010a), at different depths covering the seismogenic volume, considering all the specific cases individually or the averaged result on each grid point. But in many other cases the calculation depth for maps of Coulomb stress is not even mentioned and this parameter is not given the right importance in the analysis and applications of the CFF model. We show in the following sections that the calculated stress is strongly depth dependent and that the depth of calculation can influence the forecasting ability of the model more than other *a priori* assumptions. We suggest a simple recipe for applying the CFF model in order to obtain a more reliable forecast of subsequent events, in particular we demonstrate that the best strategy for real-time applications is to select the maximum stress values over the seismogenic volume.

Our main case study is the 1997 Umbria-Marche, central Italy, seismic sequence, which struck the Umbria-Marche region, in the central Apennines. What makes this sequence particularly worthy of attention is the difficulty of explaining it in terms of stress change due to the complexity of its geological setting that often causes a mismatch between forecasts and actual events. Catalli *et al.* (2008) suggested that forecasts could perhaps be more accurate by considering further physical phenomena such as fluid flow (Miller *et al.* 2004). With our new assumptions, in particular taking into account the fundamental role of depth, we can improve substantially the predicted spatial pattern and the total number of expected triggered events for this sequence.

The Umbria-Marche sequence took place in a normal faulting environment. To corroborate the results obtained for the Umbria-Marche sequence, we compare them with the cases of the 1992 Landers, California, and the 1999 Chi–Chi, Taiwan, earthquakes, which took place in a strike-slip and thrust fault regime, respectively.

Identifying a reliable high-risk area in real time after large earthquakes is the major priority in earthquake forecasting. In all the three case studies (Umbria-Marche, Landers and Chi–Chi), our results represent a good forecast of the highest hazard area after major earthquakes, taking also into account the role of the depth. We find that in most cases these areas match with the recordings of the catalogue.

In this work the Coulomb calculations are made using the COULOMB 3.1 code (Lin & Stein 2004; Toda *et al.* 2005). We use the isotropic poroelastic setting for the CFF model in accordance with previous studies like Nostro *et al.* 2005; Catalli *et al.* 2008; Chan & Stein 2009 and references therein. The fixed value used for the apparent friction coefficient μ' is 0.4.

2 UNCERTAINTIES IN THE CFF MODEL

The calculation of stress variations, ΔCFF, is affected by assumptions—in particular locations and geometry—related to both causative and receiver fault planes. In principle, ΔCFF estimations are also influenced by some rheological parameters like the friction and the Skempton coefficients, but some previous works concluded that the influence of such parameters does not affect the results in a substantial way (Cocco & Rice 2002; Chan & Stein 2009), when they vary within a realistic range.

2.1 Focal mechanism of receiver events

The focal mechanisms of receiver events have an indisputable influence when estimating stress changes. Because of the difficulty to predict the exact mechanisms of subsequent events, one has to make an *a priori* hypothesis. The simplest assumption one can make is to identify a prescribed mechanism, considering that usually subsequent events present geometrical characteristics similar to those of the causative main shock. This assumption is inappropriate when one studies an area where different mechanisms are triggered by a mainshock (Ma *et al.* 2005). Steacy *et al.* (2005a,b) and Hainzl *et al.* (2010a) noted that usually the mechanisms of aftershocks show a large variability. Another possibility is to use OOPs, that is those planes where the sum of stress changes (due to the causative main shocks) and the regional stress in the area reaches its maximum value. In some cases this assumption can noticeably change the shape and the total number of expected events, visibly improving the forecast, particularly near the causative fault or on the same fault plane by reducing stress shadow areas (Cocco *et al.* 2010). Using OOPs, however, a further free parameter, the regional stress field, is introduced in the calculation. Coulomb stress calculations are affected by the regional stress magnitude for a given earthquake stress drop, in particular near the mainshock fault plane (King *et al.* 1994). For instance, if the regional deviatoric stress is much larger than the

stress change imparted by earthquakes, the orientations of the optimum slip planes are more limited, and the area of increased stress diminishes in size and becomes more isolated from the causative fault. We should also note that in some cases the predicted OOPs do not agree with many of the aftershock solutions for the studied area (Nostro *et al.* 2005). This shows the difficulty in predicting aftershocks fault plane solutions while at the same time having to account for constraints from structural geology (McCloskey *et al.* 2003).

Hainzl *et al.* (2010a) suggest calculating ΔCFF for multiple receiver fault orientations. They demonstrate that, in the presence of multiple receiver fault planes, the aftershock productivity increases significantly and stress shadow areas tend to decrease. They describe the orientation of receiver faults using a distribution function. In accordance with Hainzl *et al.* (2010a), we show in this work the benefit of using receiver fault planes whose strike, dip and rake are spatially variable. However, we limit their variability using focal mechanisms compatible with geological observations, as previously suggested by Chan *et al.* (2010) and Toda *et al.* (2008). In this way we preserve the variability for possible receiver faults, at the same time constraining them, using actual observations.

Once we identify the target fault plane solution, unless we know which nodal plane corresponds to the orientation of the geological fault plane, we still have to take into account the possible uncertainty related to the calculation of ΔCFF for the two different nodal planes (the real one and the auxiliary one). Following Chan & Stein (2009), for each grid node we evaluated ΔCFF upon the two nodal planes and we randomly selected one of the two values for 10 times to work out an average of ΔCFF.

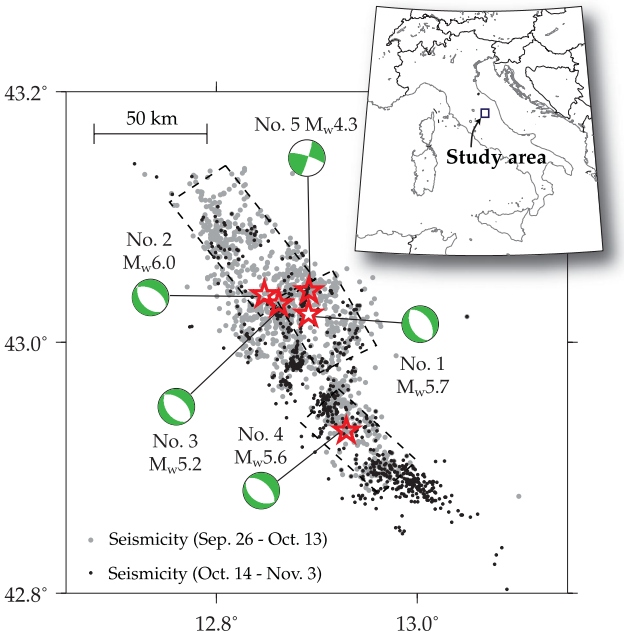

Figure 1. Distribution of seismicity (Chiarabba & Amato, 2003) and fault plane solutions of the main earthquakes (Hernandez *et al.*, 2004) of the 1997 Umbria-Marche, central Italy, seismic sequence listed in Table 1 and used for calculations. Grey dots represent $M \geq 2.5$ seismicity observed between September 26 and October 13. Black dots represent $M \geq 2.5$ subsequent seismicity, until November 3. The dashed lines represent fault-edge projections of the two mainshocks of September 26 and the event of October 14.

2.2 Depth of calculation

Unless the station network is dense and the minimum epicentral distance is small, focal depth uncertainties are large. Focal depth errors are due both to random arrival time errors and to systematic errors from poorly known seismic velocities. So it is clear that the depth of the causative events used for ΔCFF calculations is affected by significant uncertainties. These uncertainties are problematic because the CFF model is very sensitive to the relative depth between source and receiver. Cross-sections of Coulomb stress changes for a vertical strike-slip fault and for a normal fault clearly show how stress change shapes vary with depth, turning from positive to negative values and viceversa (see fig. 2 in Nostro *et al.* (1997) for a general understanding and Figs 6, 10 and 13 in the following sections for specific cases).

If ΔCFF is calculated only for a single fixed depth, one sometimes observes aftershocks occurring in area of negative expected stress changes (Nostro *et al.* 2005; Catalli *et al.* 2008). To explain these discrepancies, one can invoke (i) OOPs for ΔCFF calculations (Cocco *et al.* 2010); (ii) small-scale slip and stress heterogeneities (Marsan 2006; Helmstetter & Shaw 2006); (iii) other phenomena like the presence of fluid flow or pore pressure relaxation. Although such assumptions improve the forecating ability of the ΔCFF model, they introduce more complexity and additional uncertainties.

In this paper we propose an alternative strategy that not only provides forecasts that are more consistent with observations, but which is also simpler to implement in real-time applications. This strategy consists of mapping the maximum ΔCFF value calculated for different depths over the entire seismogenic volume, in accordance with the assumption that seismicity will occur at the location and depth where the stress is most increased toward failure (Mendoza & Hartzell 1998; Toda *et al.* 2005). This procedure takes into account that we do not know the exact depth of either the causative faults or subsequent events.

As we demonstrate in the following application to the Umbria-Marche sequence, this method allows us to map the areas of highest aftershock hazard in a simple and reliable way.

Table 1. Locations, magnitudes and fault plane solutions of the three largest events of the 1997 Umbria-Marche sequence used for ΔCFF computations (highlighted in grey) and of two of the events studied in the work (for the complete list of main shocks and details on the sequence refer to Catalli *et al.* (2008) and references therein).

ID	Date	Longitude °E	Latitude °N	Length (km)	Width (km)	Depth (km)	M_w	Strike (deg)	Dip (deg)	Rake (deg)
1	1997–09-26	12.8917	43.0225	7	7	5.7	5.7	152	46	−83
2	1997–09-26	12.8622	43.0305	12	7	5.7	6.0	144	42	−80
3	1997–10-03	12.8475	43.038	5	5	4.82	5.2	141	43	−74
4	1997–10-14	12.9296	42.9293	9	6	5.98	5.6	122	38	−100
5	1997–10-16	12.8921	43.0411	1.5	1.5	0.94	4.3	287	80	175

3 THE 1997 UMBRIA-MARCHE SEQUENCE

3.1 Overview

The 1997 Umbria-Marche seismic sequence struck the region of Central Apennines in Italy (Fig. 1). The main shocks of the sequence ruptured NW-SE normal faults dipping in the direction of the Tyrrhenian see, in accordance with the extensional tectonics active in this sector of the Apennines. The focal mechanisms of these shocks are shown in Fig. 1 and all the source parameters of the $M \geq 5.5$ main shocks used in our computations are listed in Table 1.

The seismic sequence began on September 3 with a M_w 4.5 foreshock. The two largest events of the sequence (M_w 5.7 and 6.0)

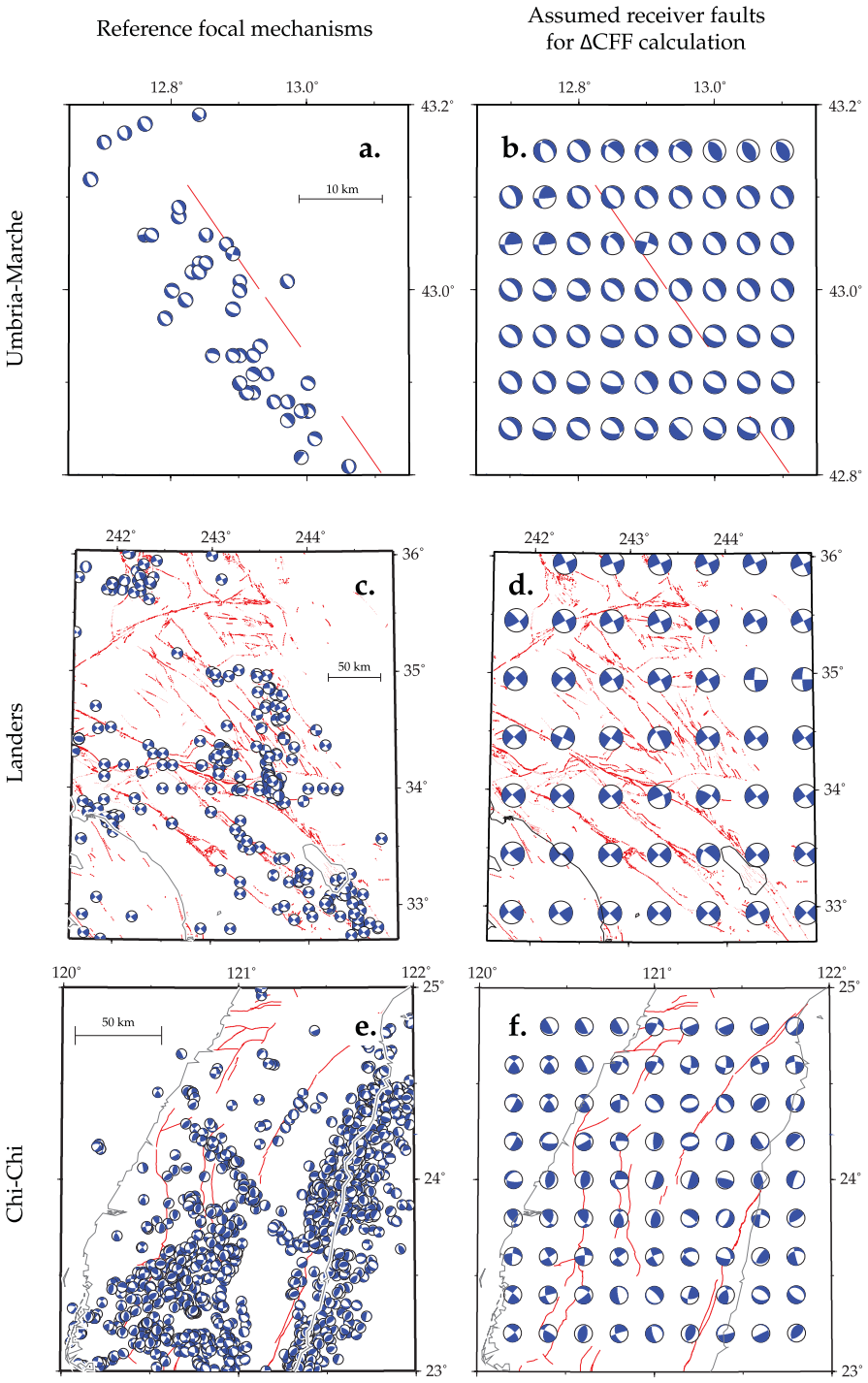

Figure 2. Reference focal mechanisms (a) for the Umbria-Marche area from the INGV-Harvard European-Mediterranean RCMT Catalogue during 1977–2006 with depth in between 0 and 20 km; (b) for the Landers area by Wang *et al.* (2009) during 1800–1992 with depth in between 0 and 10 km; and (c) for the Chi–Chi area by Wu *et al.* (2008) during 1991–1999 with depth in between 0 and 30 km. Panels (b), (d) and (f) represent relative spatially variable receiver faults for the three studied areas. Note that the spacing of the focal mechanisms in this figure is sparser than the actual grid for the Coulomb stress calculation. Red lines represent active faults.

struck the area on September 26 and ruptured two normal faults with opposite rupture directivity (Pino *et al.* (1999) and Hernandez *et al.* (2004)). In the following 18 days these events were followed by other four earthquakes of moderate magnitude ($5.0 < M_w < 6.0$), which also ruptured normal fault segments. On October 3 a normal faulting earthquake (M_w 5.2, the event number 3 in Fig. 1) occurred either in the hanging wall of the previous main causative faults or on the same fault segment that had ruptured during the September 26 (0940 UTM) main shocks and within the high slip patch (Nostro *et al.* 2005). The particular position of this event makes its forecast through stress change calculations especially difficult because it occurred in a typical stress shadow area. On October 16 a strike-slip earthquake (M_w 4.3, event number 5 in Fig. 1) ruptured a nearly NS shallow structure inherited by previous tectonics (Collettini *et al.* 2005). The progressive activation of fault segments ranging between 5 and 12 km, made up a broad, ∼45 km long, NW-trending fault system. The geometry of each segment consists of a planar fault, dipping toward SW with an average dip of 40°–45° (Amato *et al.* 1998; Chiaraluce *et al.* 2003) down to 8 km depth. The largest magnitude earthquakes of the sequence nucleated at the base of the seismogenic volume (5–6 km).

Despite the evident migration of hypocenters to the southeast, a relevant seismic activity has been detected in the epicentral area of the September 26 main shocks during the whole sequence. Chiaraluce *et al.* (2003) pointed out the presence of normal faulting aftershocks on the hanging wall of the main shock fault planes and the lack of seismicity on the footwall. However, according to the Coulomb model the hanging wall of a normal fault is characterized by a volume of negative variation of the stress close to the source plane (see fig. 2b in Nostro *et al.* (1997)). Aftershock nucleation is therefore inhibited in this volume. If ΔCFF are calculated onto a fixed depth crossing the fault plane, numerous aftershocks observed on the hanging wall of the fault planes remain unexplained (Nostro *et al.* 2005; Catalli *et al.* 2008).

Following Nostro *et al.* (2005) and Catalli *et al.* (2008), we use the available non-uniform slip distributions on the fault plane for the three largest events of the sequence (the two events of September 26 and the October 14 earthquake) obtained by Hernandez *et al.* (2004) by the inversion of GPS, DInSAR and strong motion data. We use the focal mechanisms collected in the time window 1977–2006 in the INGV-Harvard European-Mediterranean Regional Centroid Moment Tensor (RCMT) Catalogue (Pondrelli *et al.* 2006) as reference receiver faults for estimating spatially variable strike, dip and rake for the receiver faults. We also consider the focal mechanisms after 1997 because the catalogue only contains data related to a small number of earthquakes that happened before 1997 and an insignificant change of regional stress is expected after the Umbria-Marche sequence. In accordance with the nearest available reference focal mechanism in this database, as shown in Fig. 2, we assume a different receiver fault plane for all 2050 grid-cells with dimension of $0.01° \times 0.01°$.

When a prescribed receiver focal mechanism is rather used, we fix it in accordance with Catalli *et al.* (2008), using the mean value for the strike, dip and rake angles observed in the sequence (i.e. strike = 149°; dip = 46°; rake = −93°). For ΔCFF solved on OOPs, we assumed the trend, plunge and relative amplitude of the stress tensor (Table 2) obtained by Chiaraluce *et al.* (2003). We used the precise relocations obtained by Chiarabba & Amato (2003) from their 3-D tomographic study of the area to map the spatial pattern of seismicity during the 1997 seismic sequence. This catalogue includes events from 1997 September 26 to November 3.

Table 2. Regional stress tensor used to calculate Coulomb stress on OOPs in the Umbria-Marche area. The listed trend, plunge and relative amplitude of the stress tensor are obtained by Chiaraluce *et al.* (2003).

Stress directions	Azimuth (deg)	Inclination (deg)	Magnitude (bar)
$\sigma 1$	160.77	75.29	20
$\sigma 2$	−37.96	13.89	0
$\sigma 3$	53.10	4.55	−20

Nostro *et al.* (2005) and Catalli *et al.* (2008) have already tried to explain the spatio-temporal behaviour of the 1997 Umbria-Marche seismic sequence by using the CFF model, but the massive presence of aftershocks in stress shadow areas close to the causative fault planes remained mostly unexplained. The model also failed to forecast the mainshock of October 3 (event number 3 in Fig. 1). In these works a fixed depth has been used to project ΔCFF estimations by the Coulomb model. Some improvements are noted by Nostro *et al.* (2005) by introducing OOPs in the procedure and varying the depth of calculation in relation to the receiver fault depths (i.e. depth of next main event). However, they also noted that the OOPs do not fully agree with the real fault plane solutions, even when obtained using different structural constraints. Such inability to reliably duplicate aftershock mechanisms might be due to the combined uncertainties of the main shock slip model, the regional stress field and the aftershock locations (Kilb *et al.* 1997).

3.2 Stress change computations and analysis

We calculate ΔCFF imparted by the $M \geq 5.5$ earthquakes, neglecting minor stress perturbations due to the smaller events, and selecting the fault plane solution for strike, dip and rake closer to the regional predominant mechanism.(i.e. NW-SE oriented, west dipping vertical normal faults with a dip angle of *ca.* 45°).

In Fig. 3 we show stress change calculations considering as causative events the two mainshocks of September 26 (left-hand maps) and also the event of October 14 (right-hand maps) calculated for (i) a prescribed receiver fault plane (panels a–b), (ii) OOPs (panels c–d) and (iii) spatially variable receiver fault planes (panels e–f). The depth of calculation is fixed at 6 km, so to intersect every main causative fault. We can observe that in the first case (fixed receiver fault, Figs 3a and b), we are not able to forecast an important part of aftershocks (over 40 per cent of the total observed events), which seems to occur in stress shadow areas. Introducing OOPs and keeping the depth fixed (Figs 3c and d) the situation does not change visibly. To observe a significant improvement by using OOPs one has also to tune the depth of projection, as done by Nostro *et al.* (2005). Using spatially variable receiver faults (Figs 3e and f), positive ΔCFF areas show a better match with observation. In particular, we are able to forecast also the event of October 16 (event number 5 in Fig. 1), which is the only strike-slip event during this sequence. The event of October 3, which occurred on the hanging wall of the September 26 rupture plane, remains in a stress shadow area.

To validate the results shown in Fig. 3, we compare the distribution of ΔCFF with the distribution of observed aftershocks using a Molchan diagram (Molchan 1990; Molchan 1991; Zechar & Jordan 2009) as shown in Fig. 4(a). A Molchan diagram displays the rate of space occupied by alarms versus the rate of failures-to-predict (Zechar (2010)). This diagram relates distribution of ΔCFF (on the *x*-axis) to the locations of observed events (on the *y*-axis). For each

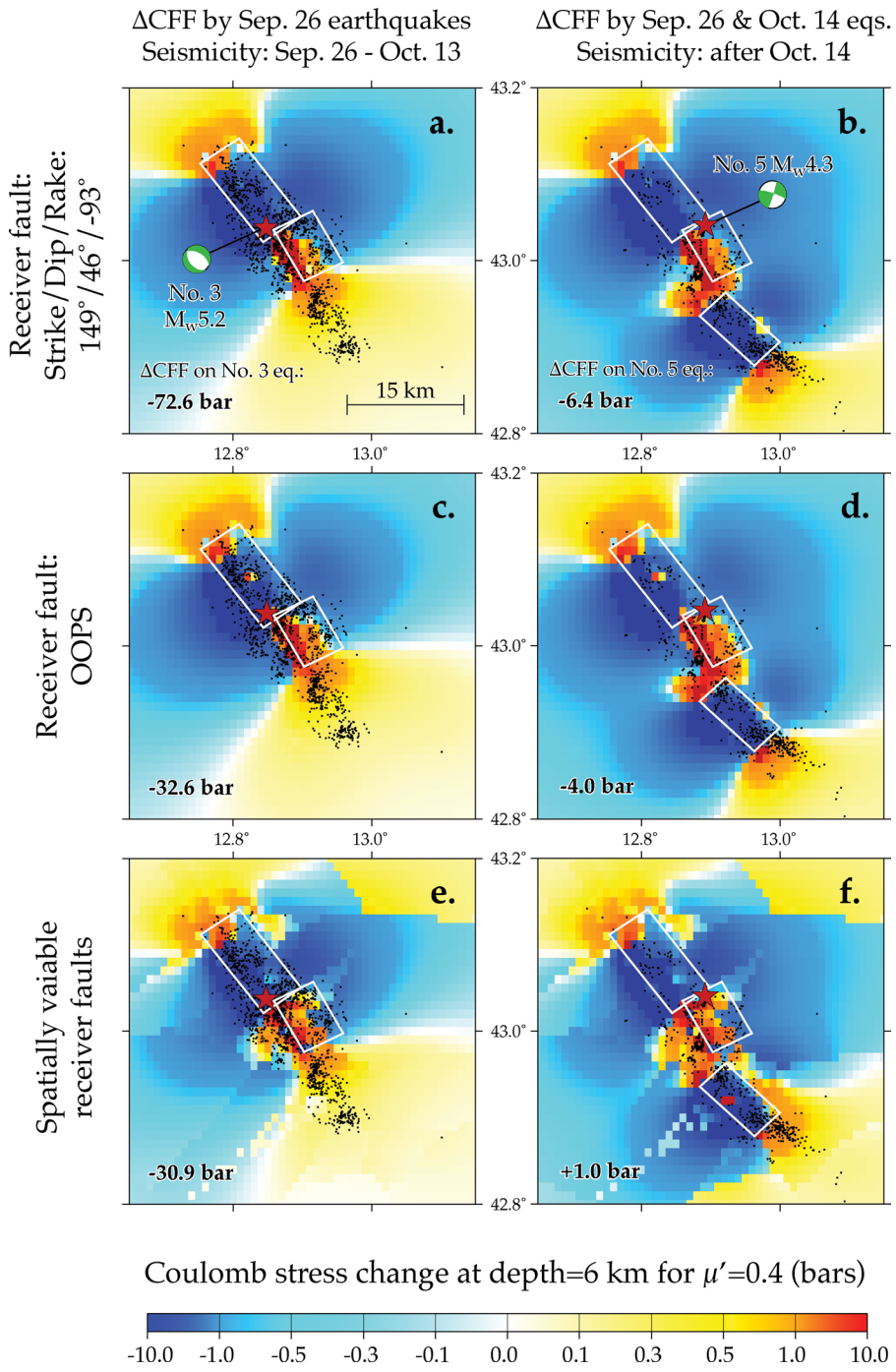

Figure 3. Maps of ΔCFF (bars) solved at 6 km depth for the Umbria-Marche, central Italy, area caused by (left-hand panels) the September 26 mainshocks (events 1 and 2 in Table 1)—and—(right-hand panels) the October 14 mainshock (events 1, 2, and 4 in Table 1). Observed seismicity with $M \geq 2.5$ (Chiarabba & Amato, 2003) for the two different time windows is superimposed on the maps (black dots). Panels (a)–(b) show ΔCFF calculated onto a prescribed receiver fault, while panels (c)–(d) show results considering OOPs and panels (e)–(f) refer to spatially variable receiver faults (considering only the nodal plane closest to the regionally predominant focal mechanism). The October 3 (event number 3) and 16 (event number 5) events are represented by red stars. In the left-bottom corner of each map is reported the local ΔCFF value relative to the location of the last mainshock occurred.

event, the total area having a ΔCFF equal to or larger than that at the location of the earthquake is selected and represented as a percentage of the total study area. The events are then sorted in agreement with the percentage of area and plotted versus event count, represented as the percentage of the total number of subsequent events. When the diagram shows a diagonal line, it means that there is no correlation between ΔCFF and subsequent seismicity. When a concave line is observed, it implies a positive correlation, and vice-versa. The optimal result would be represented by the condition of having the lowest fraction of space occupied by alarms with the lowest percentage of failure to predict. We calculate ΔCFF on all the 2050 grid-cells with dimension of $0.01^\circ \times 0.01^\circ$ considering the two

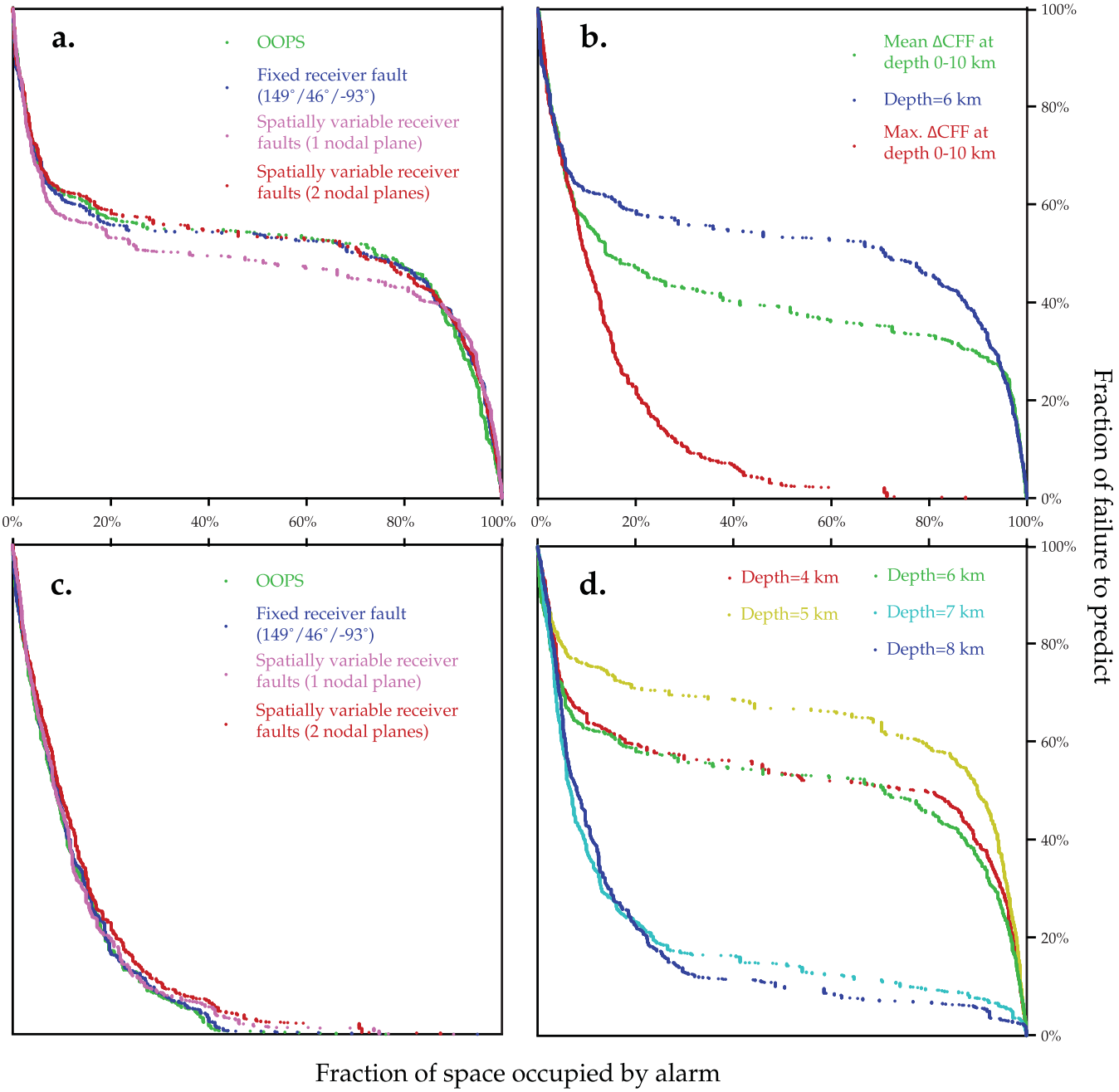

Figure 4. Molchan diagrams showing the correlation between stress changes and occurrence of aftershocks in the Umbria-Marche, central Italy, area. Panel (a) shows correlations obtained for ΔCFF calculated at the prescribed depth of 6 km solved for: (blue dots) a fixed receiver fault; (green dots) OOPs; (magenta dots) spatially variable receiver faults considering one nodal plane and (red dots) both the nodal planes (in this case a mean value of ΔCFF is reported). Panel (b) shows correlations obtained for ΔCFF calculated for spatially variable receiver faults (considering only 1 nodal plane) considering: (red dots) maximum values of stress over the seismogenic thickness (0–10 km); (green dots) mean values of stress over the seismogenic thickness; (blue dots) stress changes at 6 km. Panel (c) shows correlations obtained for maximum ΔCFF calculated over the seismogenic thickness considering: (green dots) OOPs; (blue dots) a fixed receiver fault; (magenta dots) spatially variable receiver faults considering one nodal plane and (red dots) both the nodal planes. Panel (d) shows correlations obtained for ΔCFF calculated onto five different fixed depths. The chosen step in depth is equal to the resolution of the slip model.

possible nodal plane solutions for each node. We compare ΔCFF caused by the two September 26 main shocks with the distribution of subsequent events with $M \geq 2.5$ observed between September 26 and October 13. ΔCFF imparted by the October 13 event is then cumulated and compared with events between October 13 and November 3 (Fig. 4). Fig. 4(a) confirms that the greatest improvement to the model is obtained by using spatially variable receiver faults and considering one nodal plane for projecting ΔCFF (the closer to the actual, predominant regional mechanism). It means that the better our knowledge of target mechanisms is, the more reliable is the performance of the model. One can also note that at a depth of 6 km the procedure of using fixed receiver faults performs better than using OOPs. It confirms that to improve the correlation between positive stress changes and observations in the case

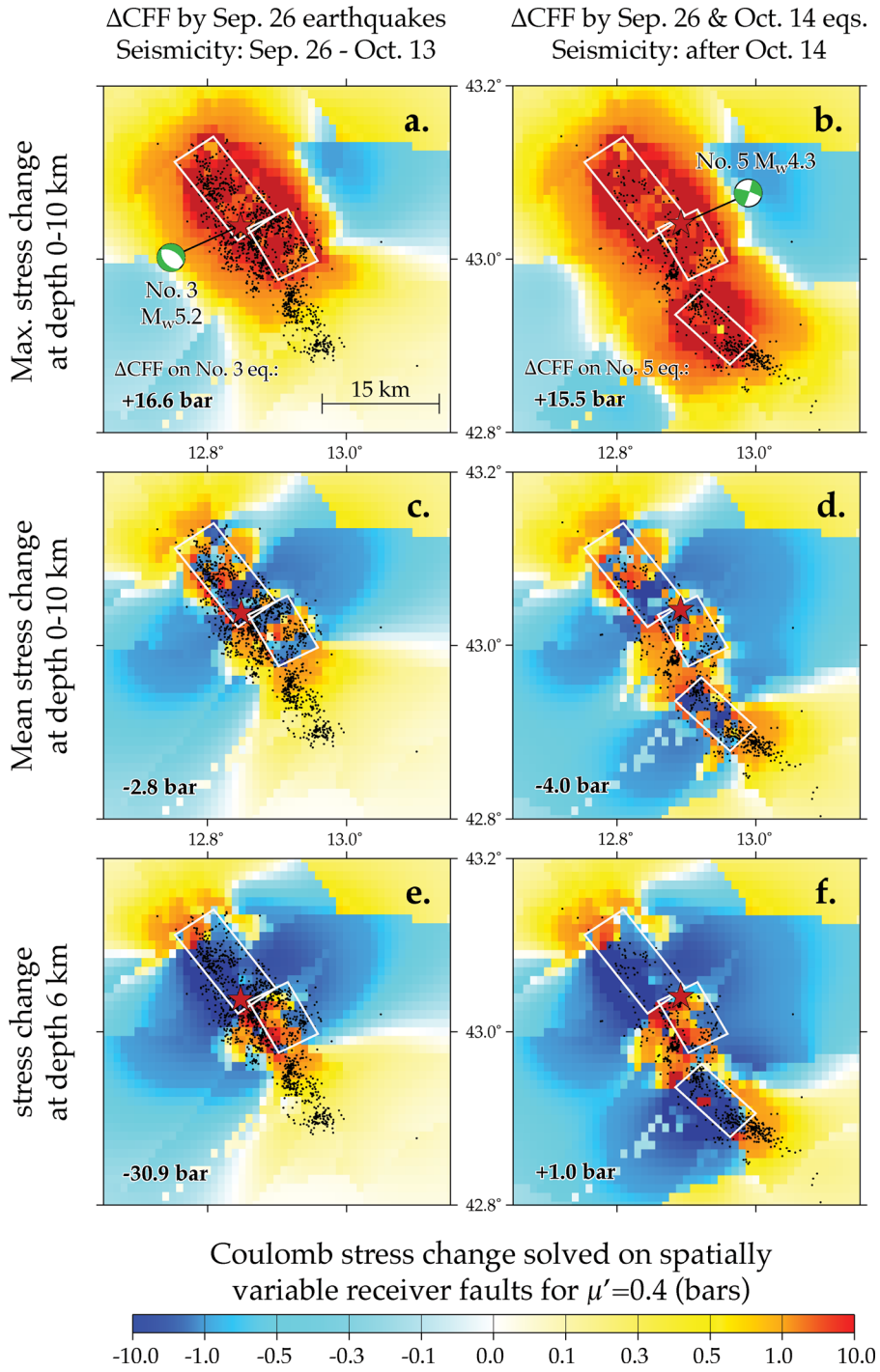

Figure 5. Maps of ΔCFF (bars) solved for spatially variable receiver faults (considering only 1 nodal plane) for the Umbria-Marche, central Italy, area caused by (left-hand panels) the September 26 mainshocks (events 1 and 2 in Table 1) and (right-hand panels) the October 14 mainshock (events 1, 2 and 4 in Table 1). Observed seismicity with $M \geq 2.5$ (Chiarabba & Amato 2003) for the two different time windows is superimposed on the maps (black dots). Panels (a)–(b) show maximum stress changes over the seismogenic thickness (0–10 km), while panels (c)–(d) show mean values of stress changes and panels (e)–(f) show ΔCFF at depth 6 km. The October 3 (event number 3) and 16 (event number 5) events are represented by red stars. In the left corner of each map is reported the local ΔCFF value relative to the location of the last mainshock.

of OOPs, we should also tune the calculation depth. However, the differences between the three approaches are rather slight.

In Figs 5 and 4(b) we show how by tuning the calculation depth we can obtain very different results. In Fig. 5 we show stress change calculations imparted by the two main shocks of September 26 (left-hand maps) and further cumulated stress changes due to the October 14 shock (right-hand maps) calculated for spatially variable receiver faults (considering the preferential nodal plane) for different depth assumptions: (i) maximum ΔCFF in the seismogenic volume (panels a–b); (ii) mean value of ΔCFF variations at different depths (panels c–d); (iii) ΔCFF at a fixed depth (panels e–f). In Fig. 5, panels (a)–(b), the improvement of positive correlations between

increasing stress areas and observed events is visibly clear when the maximum values of ΔCFF are selected over a range of depths. Fig. 4(b) confirms this improvement. We can observe that the trend of the Molchan diagram is better when we use maximum stress change. Fig. 4(c) shows another important result: the consideration of maximum stress changes is the predominant factor affecting the model performance. In this panel we focus on the case of maximum stress change values using respectively OOPs (green line), fixed receiver planes (blue line) or spatially variable planes (red line). This shows that variations in the model's performance caused by different assumptions on receiver fault solutions are almost irrelevant compared to those caused by considerations of maximum stress changes.

By using maximum values of stress changes over the entire seismogenic depth range, we can visibly improve the forecast ability of the CFF model obtaining a broader stress increasing area that matches observations. We can also forecast every main subsequent event in the sequence. Assuming each depth as a possible target area is the most effective and reliable procedure in real time, since we do not know *a priori* at which depth the next earthquakes will occur. The loss of details in terms of spatial distribution of ΔCFF, which comes along with this assumption (contours of positive/negative ΔCFF areas are visibly smoothed, panels a–b of Fig. 5) is a simplification which pays a tribute to our limited knowledge of the focal depth.

Observing the cross-section of Fig. 6 and maps of Fig. 7, we note that maximum Coulomb stress changes are selected at depth a little deeper than the bottom (or slightly above the top) of the causative faults. These regions are probable locations of aftershocks considering that aftershocks usually take place around slip asperities of mainshocks, as observed by Mendoza & Hartzell (1998). Fig. 4(d) shows a significant improvement of the model forecast ability at a depth of 7–8 km. Moreover, Fig. 4(d), together with Fig. 7, shows that the depth choice has a large impact on the results and that depth uncertainties of a few km can reduce the predictive performance by up to 50 per cent.

Of course, aftershocks can also occur on the source fault zone itself, where complexities of the slip distribution can produce spots of positive stress change. Given our limited knowledge of the actual slip distribution on the causative fault and the large focal depth uncertainties, resolving the details of the depth dependence of the ΔCFF is beyond the scope of this paper. Indeed, the proposed strategy of mapping the maximum expected ΔCFF value over the entire depth range at each point overcames the sensitivity of the CFF model to depth.

The difficulty of predicting the October 3 event, shown in Fig. 6, is another example of the important role played by depth uncertainties. The map-view of ΔCFF is shown at the prescribed depth of 6 km (Fig. 6a). In this map the examined event does not occur in an area of increasing stress. Besides, many subsequent earthquakes took place near the causative faults, where a significant drop of ΔCFF (≤ -10 bar) is estimated. Looking at the cross-section in Fig. 6(b) and at maps in Fig. 7, it is evident that forecasts obtained by estimating ΔCFF onto a fixed depth are strongly influenced by depth uncertainties.

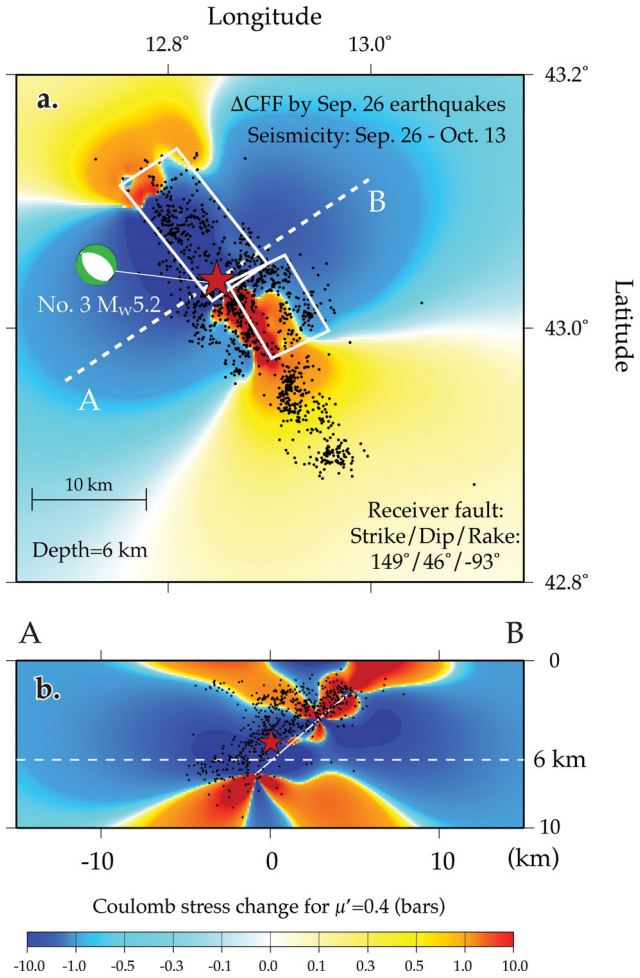

Figure 6. (a) Map and (b) cross-section of ΔCFF (bars) for analyzing the critical condition of occurrence of the October 3 mainshock (red star and relative focal mechanism). The map-view of ΔCFF is solved onto a prescribed receiver fault at 6 km depth. Subsequent actual seismicity with $M \geq 2.5$ is represented by black dots. In the cross-section all the events within 5 km from the trace are projected.

4 A COMPARISON WITH THE LANDERS AND CHI–CHI SEQUENCES

The M_w 7.3 Landers strike-slip earthquake occurred on 1992 June 28, with an epicentre located at 116.44°W longitude and 34.20°N latitude. It triggered an intense aftershock activity of more than 700 $M \geq 3$ events within the first 10 days (see the earthquake catalogue of Hauksson *et al.* (2003)). Its largest aftershock, the M_w 6.4 Big Bear event, occurred approximately 3 hr after the mainshock.

The 1992 Landers sequence has been selected by many authors as a case study, in particular to apply and study Coulomb based models, because of the availability of a large amount of fine and reliable data (Toda *et al.* 2005; Hainzl *et al.* 2009; Cocco *et al.* 2010). Many previous studies have tried to explain the Landers aftershock activity through the Coulomb model (Toda *et al.* 2005; Cocco *et al.* 2010; Hainzl *et al.* 2009 and references therein), taking into consideration also uncertainties and variability of the model itself. Hainzl *et al.* (2009) found that on average, the variability of stress calculations, independent of location, is in the order of the calculated stress values.

For the evaluation of ΔCFF imparted by the Landers main shock, we used the slip model obtained by Wald & Heaton (1994). We analyzed the relocated earthquake catalogue of Hauksson *et al.* (2003) considering earthquakes with $M \geq 2.5$, which occurred within 2 months after the main shock in the region 118.5°W to 114°W and 33.0°N to 36.0°N (SCEDC webpage at http://www.data.scec.org/research/altcatalogs.html). There are

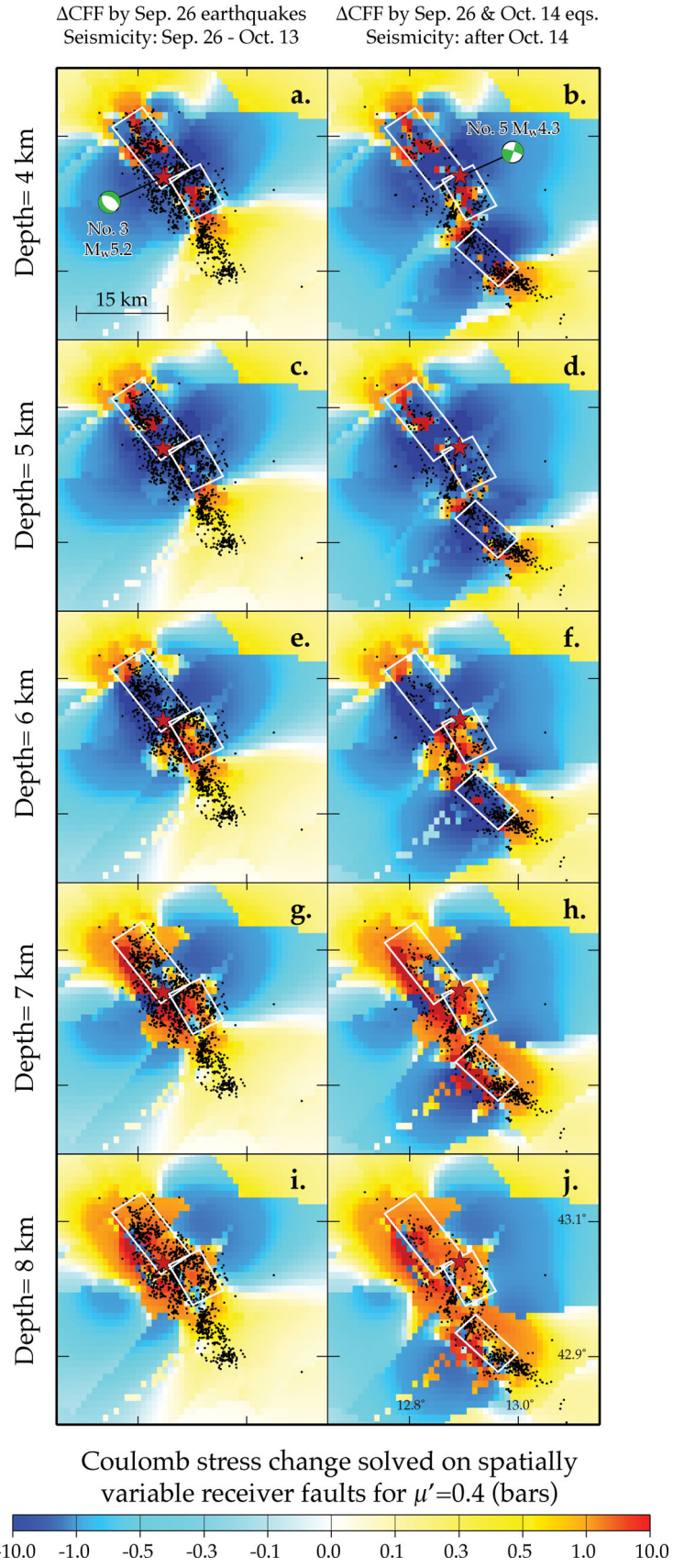

Figure 7. Maps of ΔCFF (bars) solved at five different depths, for spatially variable receiver faults (1 nodal plane) for the Umbria-Marche, central Italy, area caused by (left-hand panels) the September 26 mainshocks (events 1 and 2 in Table 1)—and—(right-hand panels) the October 14 event (events 1, 2, and 4 in Table 1). Observed seismicity with $M \geq 2.5$ (Chiarabba & Amato 2003) for the two different time windows is superimposed on the maps (black dots).

Table 3. Regional stress tensor used to calculate Coulomb stress on optimal oriented planes in the Landers area. The listed trend, plunge and relative amplitude of the stress tensor are derived from Stein *et al.* (1994).

Stress directions	Azimuth (deg)	Inclination (deg)	Magnitude (bar)
$\sigma 1$	17.00	0.00	100
$\sigma 2$	90.00	90.00	50
$\sigma 3$	107.00	0.00	0

1982 events that fit our criteria. We calculate ΔCFF on 27,723 grid cells with dimension of $0.02^\circ \times 0.02^\circ$. For ΔCFF solved on OOPs, we assumed the trend, plunge and relative amplitude of the stress tensor (Table 3) derived from Stein *et al.* (1994) and references therein. To acquire spatially variable receiver faults we use the focal mechanisms from 1800 to 1992 collected by Wang *et al.* (2009) as reference focal mechanisms (Fig. 2c) and we assume a different receiver fault plane for each grid cell (Fig. 2d), in agreement with the nearest available reference focal mechanism in this database. In the case of spatially variable receiver faults, we also consider the two possible nodal plane solutions for each node by working out a mean value of ΔCFF using the same methodology already described in the Umbria-Marche case (Fig. 9, panels a and c). However, in all the maps showing ΔCFF for spatially variable receiver fault planes also in the Landers case (as in the Umbria-Marche case) we report only values of ΔCFF calculated upon the mechanism closer to the regionally predominant mechanism, that is vertical right-lateral strike-slip with strike of 149° (Fig. 8).

Fig. 8 shows maps of ΔCFF in the area under different assumptions: (i) maximum ΔCFF over the seismogenic volume; (ii) mean stress change over the seismogenic volume; and (iii) stress changes at a prescribed depth of 7 km. In Fig. 8 it is evident that the best performance of the model is achieved by considering maximum value of ΔCFF in the seismogenic volume, without introducing any other assumption for calculations, such as OOPs or stress heterogeneities for matching observations. All the observed aftershocks, even those close to the causative fault, occur in positive stress change areas. These results are confirmed by the Molchan diagram shown in Fig. 9(b) that shows the improved forecasting ability of the model by considering maximum stress changes over the seismogenic volume. In Fig. 9(a) we observe that the hypothesis of spatially variable receiver faults, whether or not we consider the uncertainty related to the two nodal plane solutions, leads the model to perform better. Moreover, by comparing Figs 9(a) and (c) with Figs 4(a) and (c), we can observe that the ambiguity related to the calculation of ΔCFF on the two nodal planes plays a weaker role in case of a strike-slip fault system. Additionally, in Fig. 9(c) it is clear that the depth dependency is again the predominant factor and it plays a larger role than the receiver faults' dependency. Comparing Figs 4(b) and 9(b), one can also observe that under the hypotheses of (i) fixed depth and (ii) mean value of ΔCFF, the forecasting ability is worse in the Umbria-Marche than in the Landers case. This may be attributed to the fact that the distribution of ΔCFF at different depths is more homogeneous for strike-slip fault systems than for normal fault systems (see Figs 6 and 10).

In Figs 9(d) and 10 we show the impact of depth uncertainties on the forecast ability of the Coulomb model when applied in the Landers case. As for the Umbria-Marche case, we estimate that a reasonable range of depth uncertainties is represented by few kilometres. In the Landers case we can observe that the depth dependence of the forecasts is less significant than in the case of

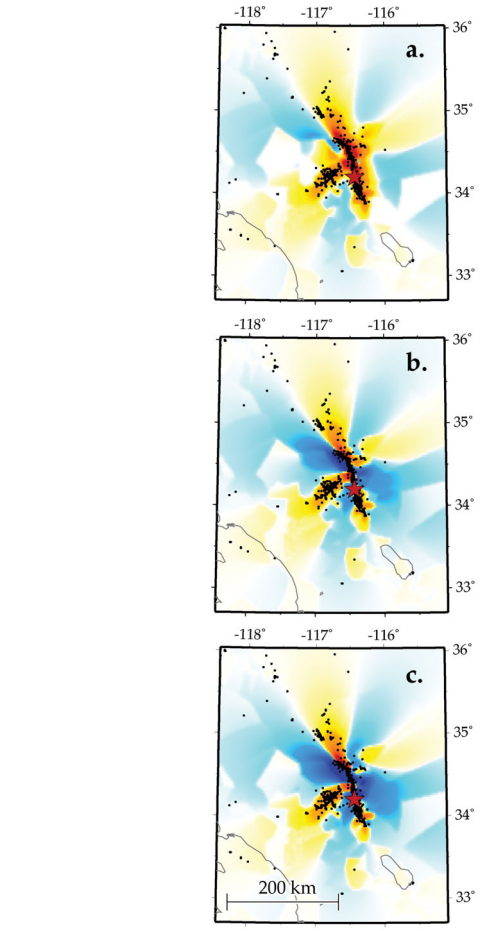

Figure 8. Maps of ΔCFF (bars) solved for spatially variable receiver faults (considering only the nodal plane closest to the regionally predominant focal mechanism) for the Landers, California, area caused by the 1992 M_w 7.3 mainshock (red star) considering: (a) maximum stress changes over the seismogenic thickness (0–15 km); (b) mean values of stress changes over the seismogenic thickness (c) stress changes at 7 km depth. Observed seismicity with $M \geq 2.5$ (Hauksson *et al.* 2003) within 2 months after the main shock is superimposed on the maps (black dots).

Umbria-Marche. In Fig. 9(d) we can see an improvement of the order of less than 10 per cent in the model's performance for a depth difference of 3 km, whereas in the Umbria-Marche case (Fig. 4d) the model's performance has an improvement of about 40 per cent for only 1 km in depth. This is in accordance with characteristics shown by cross-sections for the two different faulting mechanisms (Figs 6 and 10).

We conclude our study with an example of a thrust faulting system. We consider the M_w 7.6, 1999 Chi–Chi, Taiwan, earthquake, as a typical example of continental ramp-décollement systems, which exhibits evidence of Coulomb stress transfer in favouring aftershocks (Chan & Stein 2009, and references therein). The Chi–Chi earthquake occurred on 1999 September 20 with an epicentre located at 120.78°E longitude and 23.85°N latitude determined by the Central Weather Bureau Seismic Network (CWBSN). According

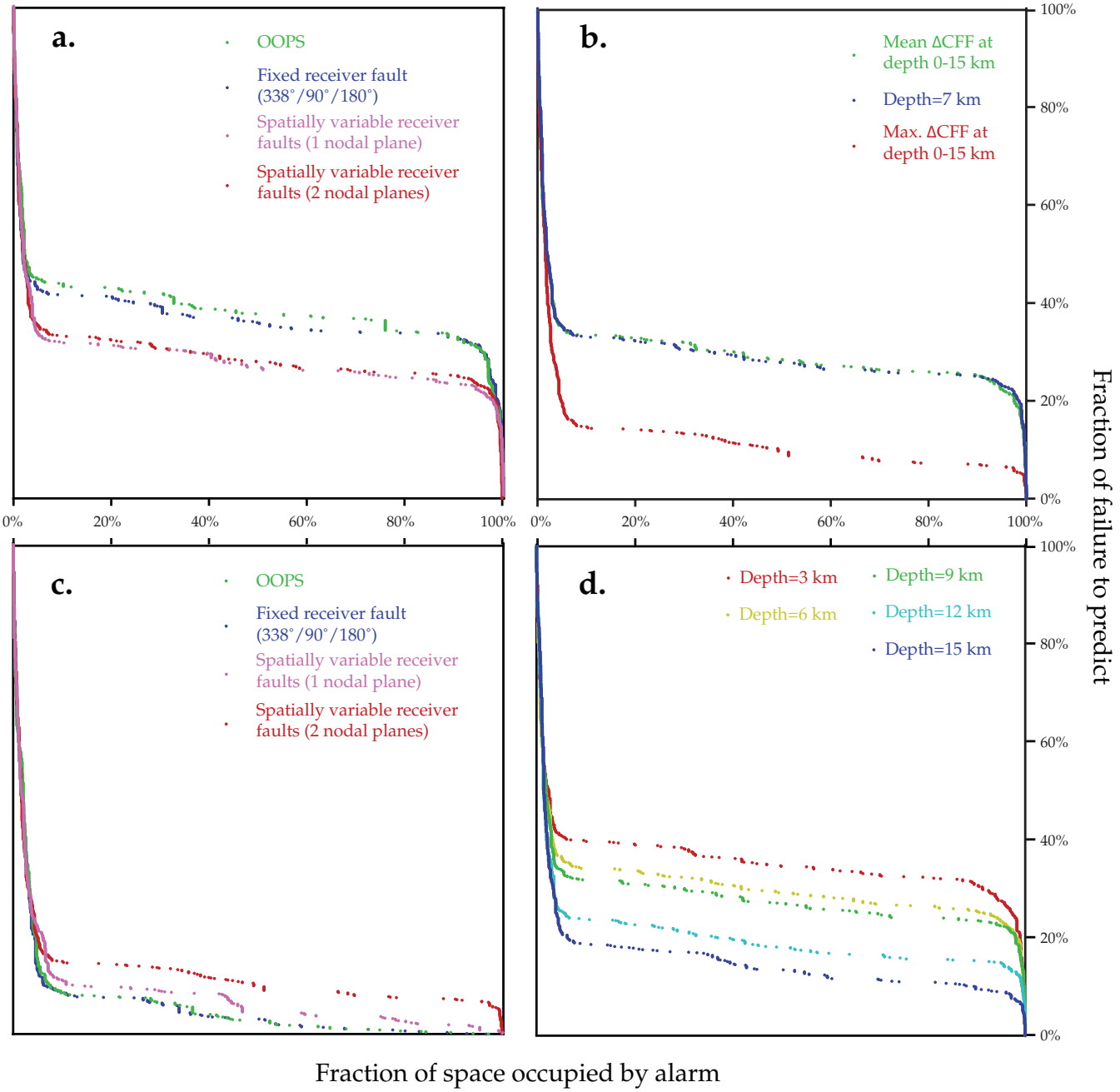

Figure 9. Molchan diagrams showing the correlation between positive stress changes and the occurrence of aftershocks in the Landers case. The four panels are organized as in Fig. 4. For the Landers case the fixed depth is 7 km and the seismogenic thickness is 0–15 km.

to the inversion of GPS observations, the coseismic slip took place along the Chelungpu fault, which dips to the East with an angle of *ca.* 30°, and with a subhorizontal décollement located at a depth of *ca.* 8 km (Johnson & Segall 2004).

We analyzed 1982 subsequent earthquakes recorded by CWBSN with $M \geq 2.0$ within 3 months after the main shock in the region 120.0°E to 122.0°E and 23.0°N to 25.0°N (Chang *et al.* 2000). The hypocentral locations of earthquakes have been relocated by Chan & Stein (2009) by using the double-difference earthquake location algorithm (hypoDD) of Waldhauser & Ellsworth (2000). To evaluate the ΔCFF caused by the main shock, we used the coseismic slip model of Johnson & Segall (2004). We calculate ΔCFF on 10,100 grid cells with dimension of 0.02° × 0.02°. For ΔCFF solved on OOPs, we assumed the trend, plunge and relative amplitude of the stress tensor (Table 4) obtained by Seno (1977). To acquire spatially variable receiver faults we use focal mechanisms collected by Wu *et al.* (2008) within the time window 1991–1999 (Fig. 2e). We assumed a different receiver fault plane for each grid cell (Fig. 2f) in agreement with the nearest available reference focal mechanism in this database. For each cell we also took into account the fault plane ambiguity by evaluating the mean value of ΔCFF after ten random calculations for one of the two nodal planes. The methodology is the same as used in the Umbria-Marche and in the Landers cases. However in the Chi–Chi case, where it is particularly difficult to

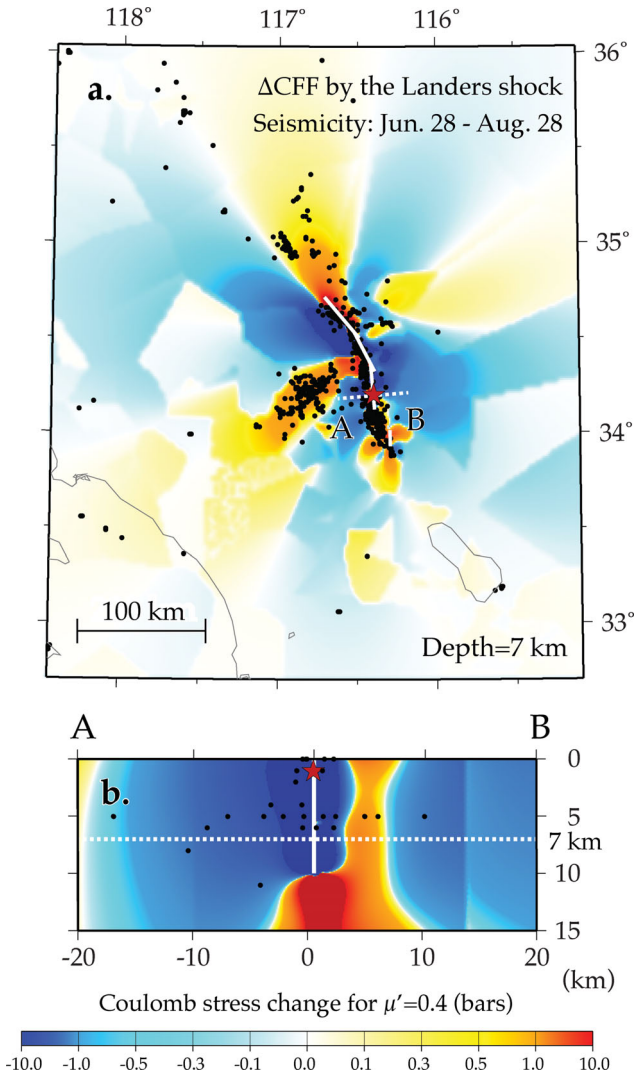

Figure 10. (a) Map and (b) cross-section of Coulomb stress changes (bars) imparted by the 1992 Landers earthquake. The map-view of ΔCFF is solved onto a prescribed receiver fault at 7 km depth. Subsequent actual seismicity with $M \geq 2.5$ is represented by black dots. In the cross-section all the events within 5 km from the trace are projected.

Table 4. Regional stress tensor used to calculate Coulomb stress on optimal oriented planes in the Chi–Chi area. The listed trend, plunge and relative amplitude of the stress tensor are obtained by Seno (1977), for the study area.

Stress directions	Azimuth (deg)	Inclination (deg)	Magnitude (bar)
$\sigma 1$	122.00	0.00	100
$\sigma 2$	32.00	0.00	30
$\sigma 3$	122.00	90.00	0

identify the geological nodal plane because of the very complex geological setting of the area, the procedure of selecting the mean value of ΔCFF plays a fundamental role because it allows us to obtain a more general and reliable result. For this reason in the Chi–Chi case in all the maps that show ΔCFF on spatially variable receiver fault planes (Figs 11 and 13)—and not only in the Molchan diagrams (Fig. 12, panels a and c)—we plotted at each node the mean value of ΔCFF worked out by considering the two possible solutions for the real plane and the auxiliary one. In Fig. 11 we show maps of stress changes for three different assumptions: (i) maximum ΔCFF over the seismogenic depth; (ii) mean stress change over the seismogenic depth; and (iii) ΔCFF at a prescribed depth of 10 km. As seen in the cases of Umbria-Marche (a normal faulting system) and Landers (a strike-slip event), in the Chi–Chi case (a thrust fault system) it is also evident that the model's best performance is obtained by selecting maximum stress changes over the entire depth range. The results are quantified in Fig. 12 where the Molchan diagrams are shown. However, in Figs 12(a) and (c) we observe a substantial difference for the Chi–Chi earthquake: these panels show that spatially variable receiver fault planes perform worse than the two other hypotheses (OOPs and fixed receiver fault planes). This behaviour can be attributed to the very different focal mechanisms that characterize the area before and after the occurrence of the Chi–Chi earthquake. Wu *et al.* (2010) found that the regional stress in this area is disturbed by the Chi–Chi main shock and they observed a rotation of the horizontal stress component, which rotated of 20° immediately after Chi–Chi. In the perspective of a real-time application of the model, we considered pre-Chi–Chi events as the reference focal mechanism for spatially variable receiver faults (Figs 2e and f). But these reference mechanisms are quite different from actual postseismic mechanisms in this area. This can represent a drawback of our approach of considering spatially variable receiver faults, especially for large events, because they cause significant disturbance of regional stress. In Fig. 12(a) it is also evident that in the case of Chi–Chi, considering the ambiguity related to the two indistinguishable nodal planes leads to an increase in the forecasting ability of the model. We gather from this result that, when we do not know the actual plane of slip, accounting for the uncertainty of the two possible solutions for ΔCFF results in a better solution. Fig. 12(b) confirms that the strategy of adopting maximum stress changes increases the forecasting ability of the model. Finally, Fig. 12(d) shows that in the Chi–Chi case depth uncertainty plays a minor role compared to the Umbria-Marche or Landers cases. This fact is also related to different distributions of focal mechanisms before and after the mainshocks. The two latter regions (Landers and Umbria-Marche) are characterized by a uniform distribution of regional stresses in accordance with distribution of reference focal mechanisms. In Figs 2(a)–(d) we can observe that similar focal mechanisms are assumed for causative and receiver faults. In those cases positive ΔCFF is obtained at a depth a little deeper than the bottom (or slightly above the top) of the causative faults (Figs 6b and 10b). The Chi–Chi case, on the other hand, is characterized by a coseismic slip that takes place along a ramp-décollement system covering different tectonic regions. The actual focal mechanisms in this case vary strongly with location (Fig. 2e). Therefore, the Chi–Chi case presents a complex ΔCFF pattern on spatially variable receiver faults. In addition we note an insignificant increase of ΔCFF beneath the décollement (Fig. 13).

5 DISCUSSION AND CONCLUSIONS

The Coulomb model is considered one of the most powerful and straightforward physics-based methods to forecast triggered seismicity (Stein 1999; Toda & Stein 2003; Toda *et al.* 2005). Nevertheless, as recently pointed out by Hainzl *et al.* (2010a and b), stress calculation is affected by a number of unsolved problems that lead to large uncertainties, such as: (i) the unknown distribution of receiver faults (McCloskey *et al.* 2003; Steacy *et al.* 2005b); (ii) the non-unique inversions for the causative slip-models (Steacy *et al.* 2004); (iii) inestimable slip variability that leads to strong stress heterogeneities close to the source fault (Marsan 2006; Hainzl &

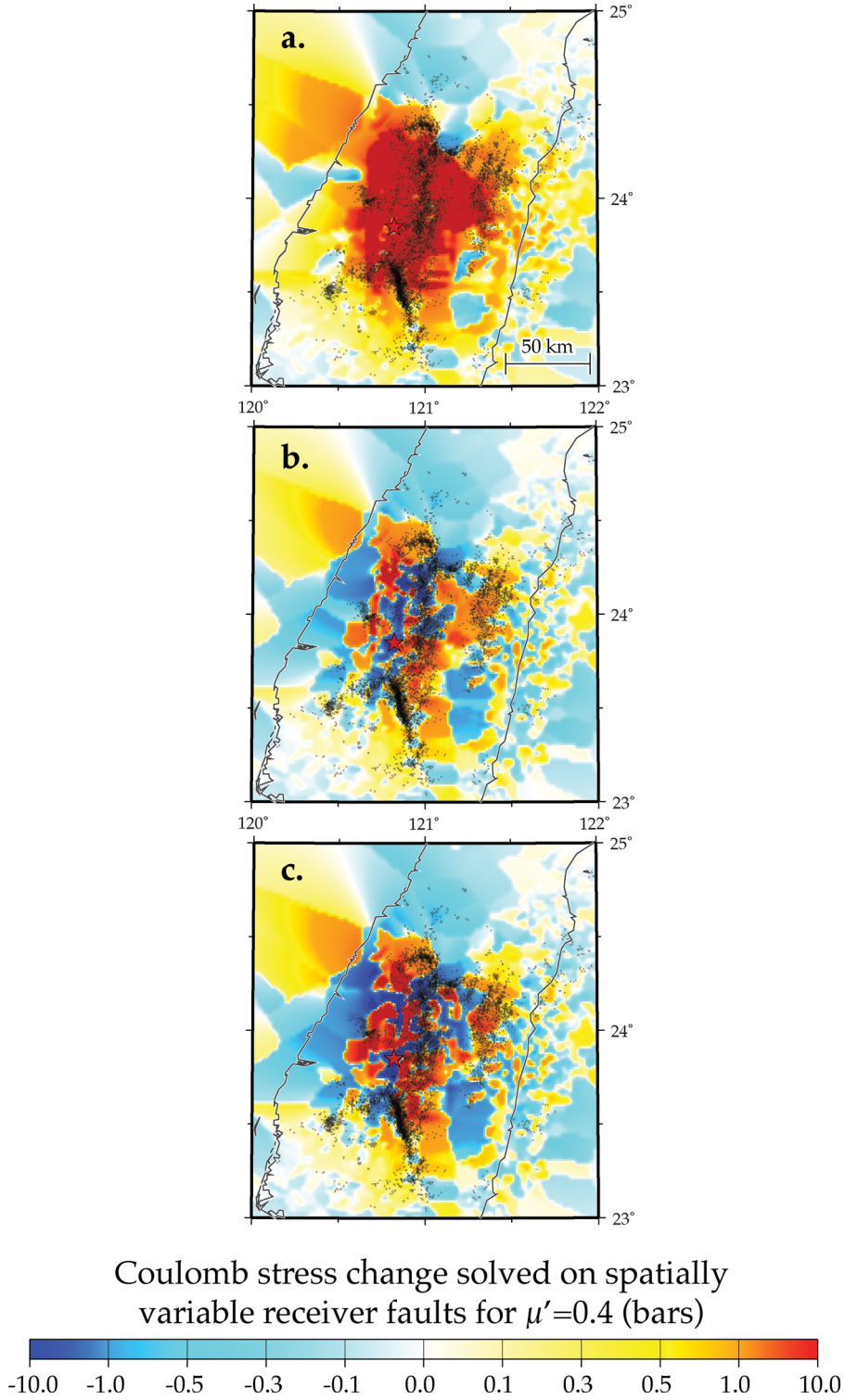

Figure 11. Maps of ΔCFF (bars) solved for spatially variable receiver faults for the Chi–Chi, Taiwan, area caused by the 1999 M_w 7.6 main shock (red star) considering: (a) maximum stress changes over the seismogenic thickness (0–30 km); (b) mean values of stress changes over the seismogenic thickness; (c) stress changes at 10 km depth. For each node the mean value of ΔCFF is reported considering the two possible nodal plane solutions. Relocated seismicity with $M \geq 2.0$ for the 3 months after the main shock (Chan & Stein 2009) is superimposed on the maps (black dots).

Marsan 2008), and (iv) spatial heterogeneity of rocks and pre-stress conditions. For all these reasons, calculated stress and observed seismicity do not always match (Hardebeck *et al.* 1998). One typical problem is that aftershocks occur also where stress shadows are evaluated (Marsan 2003; Mallman & Zoback 2007). In fact, areas of pure quiescence are rarely observed in aftershock sequences. For this reason Wössner *et al.* (2011) concluded that the CFF based models, which introduce elements of stochasticity, perform better than the pure deterministic ones, because they reduce or remove stress shadows. However, we note that none of the aforementioned

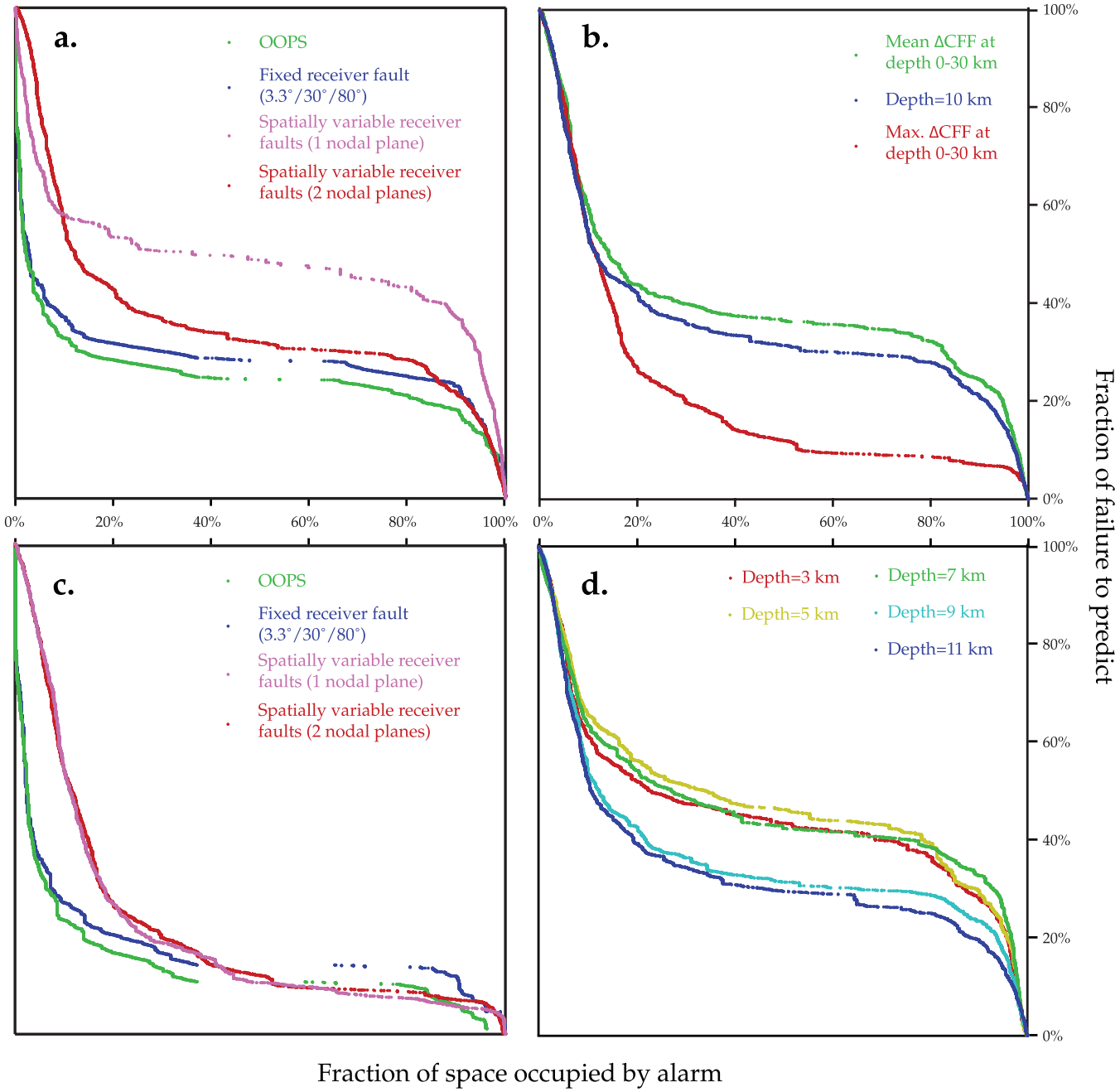

Figure 12. Molchan diagrams showing the correlation between positive stress changes and the occurrence of aftershocks in the Chi–Chi case. The four panels are organized as in Figs 4 and 9. In the Chi–Chi case the fixed depth is 10 km and the seismogenic thickness is 0–30 km. Panel (b) shows correlations obtained for ΔCFF calculated for spatially variable receiver faults considering both the nodal plane, thus the mean ΔCFF value is reported for each node.

studies discusses the role of depth when analysing or applying the CFF model.

The aim of this work is to propose an easy, practical and reliable strategy to apply the Coulomb model in real time, that improves the correlation with observed events and reduces the number of *a priori* assumptions and related uncertainties. We demonstrate that the depth of calculation plays a fundamental role in the CFF model and that it represents a powerful tuning parameter for varying the model's performance. When calculating variations of stress, the depth of calculation seems to have an even greater influence than other input information such as the orientation of receiver fault planes.

By taking into account the fundamental importance of depth for stress calculations, we can explain the occurrence of almost all the subsequent events in different sequences and then identify the highest risk area around a given source. We have analysed three cases with different faulting regimes: normal, strike-slip and thrust. In each case the analysis of stress maps and Molchan diagrams leads to the same conclusions: (i) the CFF model displays of a strong sensitivity to depth related uncertainties; (ii) selecting for each location the calculated maximum stress change over the entire depth range increases the forecast ability of the Coulomb model; (iii) the selection of maximum stress changes affects the final results more than assumptions about receiver fault planes.

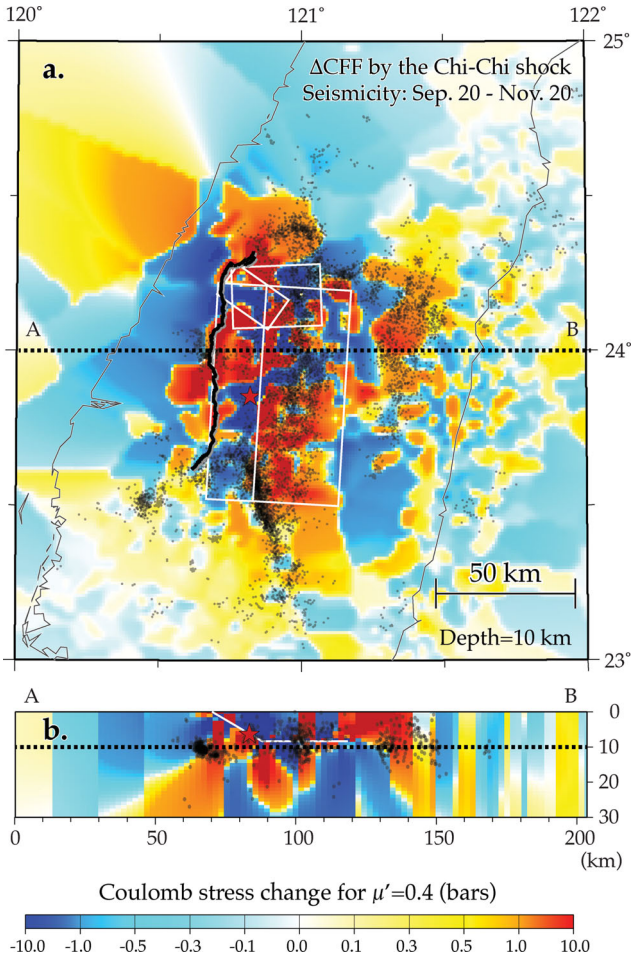

Figure 13. (a) Map and (b) cross-section of ΔCFF (bars) imparted by the 1999 Chi–Chi earthquake solved for spatially variable receiver faults (considering both the nodal planes). The map-view of ΔCFF is solved for a prescribed receiver fault at 10 km depth. Subsequent actual seismicity with $M \geq 2.0$ is represented by black dots. In the cross-section all the events within 5 km from the trace are projected.

The discussion of results obtained in the three study cases led to a further conclusion: while the benefit of assuming spatially variable receiver fault planes cannot be generalized, because it depends on the geological setting of the study area, selecting the maximum ΔCFF value at each point works in any tectonic system.

Our final conclusion is that considering the strategy of selecting maximum Coulomb stress variations improves the forecasting ability of the model more than other assumptions regarding receiver fault planes. In practice, this means a reduction of the computation time and an increase in the reliability of the results. This is in perfect accordance with the needs of real-time applications for earthquake forecasting and possible risk mitigation.

Having suggested a simplified and straightforward way to apply the deterministic CFF model, thus obtaining a good match with observations, we are aware that we have not resolved the limitations of the model in describing the details of the earthquake dynamics. We did not introduce any element of stochasticity that takes into account the model uncertainties and define its variability. We strongly believe in the urgent need to combine physics and statistics so as to advance the field of earthquake forecasting (Hainzl *et al.* 2010b and Vere-Jones 2010).

ACKNOWLEDGMENTS

We would like to thank Dr. G. Grünthal and all the group of Section 2.6 'Seismic Hazard and Stress Field' of the GFZ – German Research Centre for Geosciences. They kindly offered us their hospitality and made it possible to start this work in a stimulating environment.

FC is particularly grateful to Dr. R. Console for being always available for fruitful and illuminating discussions. We would like to thank the Editor, the two rewievers, Shinji Toda and Mark Naylor, and Nicholas Deichmann for their assistance in improving the quality of this manuscript.

REFERENCES

Amato, A. *et al*. 1998. The 1997 Umbria-Marche, Italy, earthquake sequence: A first look at the main shocks and aftershocks, *Geophys. Res. Lett.,* **25**(15), 2861–2864.

Catalli, F., Cocco, M., Console, R. & Chiaraluce, L., 2008. Modeling seismicity rate changes during the 1997 Umbria-Marche sequence (central Italy) through a rate- and state-dependent model, *J. geophys. Res.,* **113,** B11301, doi: 10.1029/2007JB005356.

Chan, C.-H. & Ma, K.F., 2004. Possibility of forecasting aftershock distributions from stress change: A case study of inland Taiwan earthquakes, *Terr. Atmos. Oceanic Sci.,* **15**(3), 503–521.

Chan, C.-H. & Stein, R.S., 2009. Stress evolution following the 1999 Chi–Chi, Taiwan, earthquake: Consequences for afterslip, relaxation, aftershocks, and departures from Omori decay, *Geophys. J. Int.,* **177,** 179–192, doi: 10.1111/j.1365-246X.2008.04069.x.

Chan C.-H., Sørensen, M.B., Stromeyer, D., Grünthal, G., Heidbach, O., Hakimhashemi, A. & Catalli, F., 2010. Forecasting Italian seismicity through a spatio-temporal physical model: Importance of considering time dependency and reliability of the forecast, *Ann. Geophys., **53,*** 3, doi:10.4401/ag-4761.

Chang, C.-H., Wu, Y.-M., Shin, T.-C. & Wang, C.-Y., 2000. Relocation of the 1999 Chi–Chi earthquake in Taiwan, *Terr. Atmos. Oceanic Sci.,* **11**(3), 581–590.

Chiarabba, C. & Amato, A., 2003. Vp and Vp/Vs images in the Mw 6.0 Umbria-Marche fault region (central Italy): A contribution to the understanding of seismotectonic and seismogenic process, *J. geophys. Res.,* **105**(B5), 2248, doi: 10.1029/2002JB002166.

Chiaraluce, L., Elsworth, W., Chiarabba, C. & Cocco, M., 2003. Imaging the complexity of an active normal fault system: The 1997 Umbria-Marche (central Italy) case study, *J. geophys. Res.,* **108**(B6), 2294, doi:10.1029/2002JB002166.

Chiaraluce, L., 2004. Complex normal faulting in the Apennines thrust and fold belt: The 1997 seismic sequence in the central Italy, *Bull. seism. Soc. Am.,* **94,** 99–116.

Cocco, M. & Rice, J.R., 2002. Pore pressure and poroelasticity effects in Coulomb stress analysis of earthquake interactions, *J. geophys. Res.,* **107**(B2), 2030, doi:10.1029/2000JB000138.

Cocco, M., Hainzl, S., Catalli, F., Enescu, B., Lombardi, A.M. & Wössner, J., 2010. Sensitivity study of forecasted aftershock seismicity based on Coulomb stress calculation and rate- and state-dependent frictional response, *J. geophys. Res.,* **115,** B05307, doi:10.1029/2009JB006838.

Collettini, C., Chiaraluce, L., Pucci, S., Barchi M. & Cocco, M., 2005. Looking at fault inversion matching structural geology and seismology data, *J. Struct. Geol.,* **27**(5), 937–942.

Field, E.H., 2007. Overview of the working group for the development of regional earthquake likelihood models (RELM), *Seism. Res. Letts.,* **78**(1), 7–16.

Hainzl, S. & Marsan, D., 2008. Dependence of the Omori-Utsu law parameters on mainshock magnitude: Observations and modeling, *J. geophys. Res.,* **113,** B10309, doi:10.1029/2007JB005492.

Hainzl, S., Enescu, B., Cocco, M., Wössner, J., Catalli, F., Wang, R. & Roth, F., 2009. Aftershock modeling based on uncertain stress calculations, *J. geophys. Res.,* **114,** B05309, doi:10.1029/2008JB006011.

Hainzl, S., Zoeller, G. & Wang, R., 2010a. Impact of the receiver fault distribution on aftershock activity, *J. geophys. Res.,* **115,** B05315, doi:10.1029/2008JB006224.

Hainzl, S., Steacy, S. & Marsan D., 2010b. Seismicity models based on Coulomb stress calculations, *Community Online Resource for Statistical Seismicity Analysis,* doi:10.5078/corssa-32035809. Available at http://www.corssa.org/articles/themev/hainzl_et_al/index.

Hardebeck, J.L., Nazareth, J.J. & Hauksson, E., 1998. The static stress change triggering model: Constraints from two southern California aftershock sequences, *J. geophys. Res.,* **103**(B10), 24427–24437.

Harris, R.A., 1998. Introduction to special section: Stress triggers, stress shadows, and implications for seismic hazard, *J. geophys. Res.,* **103**(B10), 24 347–24 358.

Hauksson, E., Chi, W.-C. & Shearer, P., 2003. Comprehensive waveform cross-correlation of southern California seismograms. Part 1. Refined hypocenters obtained using the double-difference method and tectonic implications, *EOS, Trans. Am. geophys. Un.*, **84**(46), Abstract S21D-0325.

Helmstetter, A. & Shaw, B.E., 2006. Relation between stress heterogeneity and aftershock rate in the rate-and-state model, *J. geophys. Res.,* **111,** B07304, doi:10.1029/2005JB004077.

Hernandez, B., Cocco, M., Cotton, F., Stramondo, S., Scotti, O., Courboulex, F. & Campillo, M., 2004. Rupture history of the 1997 Umbria-Marche (central Italy) largest earthquakes from inversion of GPS, DInSAR and near field seismological data, *Ann. Geophys.,* **47,** 1355–1376.

Johnson, K.M. & Segall, P., 2004. Imaging the ramp–décollement geometry of the Chelungpu fault using coseismic GPS displacements from the 1999 Chi–Chi, Taiwan earthquake, *Tectonophysics,* **378**, 123–139.

Jordan, T., 2006. Earthquake predictability, brick by brick, *Seismol. Res. Letts.,* **77**(1), 3–6.

King, G.C.P., Stein R. & Lin J., 1994. Static stress change and the triggering of earthquakes, *Bull. seism. Soc. Am.,* **84,** 935–953.

Kilb, D., Ellis, M., Gomberg, J. & Davis S., 1997. On the origin of diverse aftershock mechanisms following the 1989 Loma Prieta earthquake, *Geophys. J. Int.,* **128,** 557–570.

King, G.C.P. & Cocco, M., 2001. Fault interaction by elastic stress changes: New clues from earthquake sequences, *Adv. Geophys.,* **44,** 1–39.

Lin, J. & Stein, R.S., 2004. Stress triggering in thrust and subduction earthquakes, and stress interaction between the southern San Andreas and nearby thrust and strike-slip faults, *J. geophys. Res.,* **109,** B02303, doi:10.1029/2003JB002607.

Ma, K.-F., Chan, C.-H. & Stein, R.S., 2005. Response of seismicity to Coulomb stress triggers and shadows of the 1999 Mw = 7.6 Chi–Chi, Taiwan, earthquake. *J. geophys. Res.,* B05S19, doi:10.1029/2004JB003389.

Mallman, E.P. & Zoback, M.D., 2007. Assessing elastic Coulomb stress transfer models using seismicity rates in southern California and southwestern Japan, *J. geophys. Res.,* **112,** B03304, doi:10.1029/2005JB004076.

Marsan, D., 2003. Triggering of seismicity at short timescales following Californian earth-quakes, *J. geophys. Res.,* **108,** 2266, doi:10.1029/2002JB001946.

Marsan, D., 2006. Can coseismic stress variability suppress seismicity shadows? Insights from a rate-and-state friction model, *J. geophys. Res.,* **111,** B06305, doi:10.1029/2005JB004060.

McCloskey, J., Nalbant, S.S., Steacy, S., Nostro, C., Scotti, O. & Beaumont, D., 2003. Structural constraints on the spatial distribution of aftershocks, *Geophys. Res. Lett.,* **30**(12), 1610, doi:10.1029/2003GL017225.

Mendoza, C. & Hartzell, S.H., 1998. Inversion for slip distributions using GSDN *P* waves: North Palm Springs Borah Peak and Michoacan earthquakes, *Bull. seismol. Soc. Am.,* **78,** 1092–1111.

Miller, S.A., Collettini, C., Chiaraluce, L., Cocco, M., Barchi, M.R. & Kaus, B.J.P. (2004. Aftershocks driven by a high pressure CO2 source at depth, *Nature,* **427,** 724–727, doi:10.1038/nature02251.

Molchan, G.M., 1990. Strategies in strong earthquake prediction, *Phys. Earth planet. Inter.,* **61,** 84–98.

Molchan, G.M., 1991. Structure of optimal strategies in earthquake prediction, *Tectonophysics,* **193,** 267–276.

Nostro, C., Cocco, M. & Belardinelli, M.E., 1997. Static stress changes in extensional regimes: An application to Southern Apennines (Italy), *Bull. seism. Soc. Am.,* **82,** 1018–1040.

Nostro, C., Chiaraluce, L., Cocco, M., Baumont, D. & Scotti, O., 2005. Coulomb stress changes caused by repeated normal faulting earthquakes during the 1997 Umbria-Marche (central Italy) seismic sequence, *J. geophys. Res.,* **110**(B05S20), doi:10.1029/2004JB003386.

Pino, N.A., Mazza, S. & Boschi, E., 1999. Rupture directivity of the major shocks in the 1997 Umbria-Marche (central Italy) sequence from regional broadband waveforms, *Geophys. Res. Lett.,* **26,** 2101–2104.

Pondrelli, S., Salimbeni, S., Ekström, G., Morelli, A., Gasperini, P. & Vannucci, G., 2006. The Italian CMT dataset from 1977 to the present, *Phys. Earth planet. Int.,* **159,** 286–303.

Seno, T., 1977. The instantaneous rotation vector of the Philippine Sea Plate relative to the Eurasian Plate, *Tectonophysics,* **42,** 209–226.

Steacy, S., Marsan, D., Nalbant, S.S. & McCloskey, J., 2004. Sensitivity of static stress calculations to the earthquake slip distribution, *J. geophys. Res.,* **109,** B04303, doi:10.1029/2002JB002365.

Steacy, S., Gomberg, J. & Cocco, M., 2005a. Introduction to special section: Stress transfer, earthquake triggering, and time-dependent seismic hazard, *J. geophys. Res.,* **110,** B05S01, doi:10.1029/2005JB003692.

Steacy, S., Nalbant, S., McCloskey, J., Nostro, C., Scotti, O. & Beaumont, D., 2005b. Onto what planes should Coulomb stress perturbations be resolved? *J. geophys. Res.,* **110**(B05S15), doi:10.1029/2004JB003356.

Stein, R.S., 1999. The role of stress transfer in earthquake occurrence, *Nature,* **402,** 605–609.

Stein, R.S., King, G.C.P. & Lin, J., 1994. Stress triggering of the 1994 M = 6. 7 Northridge, California, earthquake by its predecessors, *Science,* **265,** 1432–1435.

Toda, S. & Stein, R.S., 2003. Toggling of seismicity by the 1997 Kagoshima earthquake couplet: A demonstration of time-dependent stress transfer, *J. geophys. Res.,* **108**(B12), 2567, doi:10.1029/2003JB002527.

Toda, S., Stein, R.S., Richards-Dinger, K. & Bozkurt, S.B., 2005. Forecasting the evolution of seismicity in southern California: Animations built on earthquake stress transfer, *J. geophys. Res.,* **110**(B5), B05S16, doi:10.1029/2004JB003415.

Toda, S., Lin, J., Meghraoui, M. & Stein, R.S., 2008. 12 May 2008 M = 7.9 Wenchuan, China, earthquake calculated to increase failure stress and seismicity rate on three major fault systems, *Geophys. Res. Lett.,* **35,** L17305, doi:10.1029/2008GL034903.

Vere-Jones, D., 2010. How to educate yourself as a statistical seismologist, *Community Online Resource for Statistical Seismicity Analysis,* doi:10.5078/corssa-17728079. Available at http://www.corssa.org.

Wald, D.J. & Heaton, T.H., 1994. Spatial and temporal distribution of slip for the 1992 Landers, California, earthquake, *Bull. seism. Soc. Am.,* **84**(3), 668–691.

Waldhauser, F. & Ellsworth, W.L., 2000. A double-difference earthquake location algorithm: Method and application to the northern Hayward fault, *Bull. seism. Soc. Am.,* **90,** 1353–1368.

Wang, Q., Jackson, D.D. & Kagan, Y.Y., 2009. California Earthquakes, 1800–2007: A unified catalog with moment magnitudes, Uncertainties, and focal mechanisms, *Seis. Res. Lett.,* **80**(3), 446–457; doi: 10.1785/gssrl.80.3.446.

Wössner, J., Hainzl, S., Marzocchi, W., Werner, M.J., Lombardi, A.M., Catalli, F., Enescu, B., Cocco, M., Gerstenberger M.C. & Wiemer, S. 2011. A Retrospective Comparative Forecast Test on the 1992 Landers Sequence, *J. geophys. Res.,* **116,** B05305, doi:10.1029/2010JB007846.

Wu, Y.-M., Zhao, L., Chang, C.-H. & Hsu, Y.-J., 2008. Focal-mechanism determination in Taiwan by genetic algorithm, *Bull. seism. Soc. Am.,* **98**(2), 651–661, doi:10.1785/0120070115.

Wu, Y.-M., Hsu, Y.-J., Chang, C.-H., Teng, L.S.-Y. & Nakamura, M., 2010. Temporal and spatial variation of stress field in Taiwan from 1991 to 2007: Insights from comprehensive first motion focal mechanism catalog, *Earth planet. Sci. Lett.,* **298,** 306–316, doi:10.1016/j.epsl.2010.07.047.

Zechar, J.D. & Jordan, T.H.E., 2009. The area skill score statistic for evaluating earthquake predictability experiments, *Pure Appl. Geophys.,* **167**(8/9), 893–906.

Zechar, J.D., 2010. Evaluating earthquake predictions and earthquake forecasts: A guide for students and new researchers, *Community Online Resource for Statistical Seismicity Analysis,* doi:10.5078/corssa-77337879. Available at http://www.corssa.org/articles/themevi/zechar.